Article

Viscoelastic Properties of Confluent MDCK II Cells Obtained from Force Cycle Experiments

Bastian Rouven Brückner,[1] Helen Nöding,[1] and Andreas Janshoff[1,*]

[1]Georg-August-Universität Göttingen, Institute of Physical Chemistry, Göttingen, Germany

ABSTRACT   The local mechanical properties of cells are frequently probed by force indentation experiments carried out with an atomic force microscope. Application of common contact models provides a single parameter, the Young's modulus, to describe the elastic properties of cells. The viscoelastic response of cells, however, is generally measured in separate microrheological experiments that provide complex shear moduli as a function of time or frequency. Here, we present a straightforward way to obtain rheological properties of cells from regular force distance curves collected in typical force indentation measurements. The method allows us to record the stress-strain relationship as well as changes in the weak power law of the viscoelastic moduli. We derive an analytical function based on the elastic-viscoelastic correspondence principle applied to Hertzian contact mechanics to model both indentation and retraction curves. Rheological properties are described by standard viscoelastic models and the paradigmatic weak power law found to interpret the viscoelastic properties of living cells best. We compare our method with atomic force microscopy-based active oscillatory microrheology and show that the method to determine the power law coefficient is robust against drift and largely independent of the indentation depth and indenter geometry. Cells were subject to Cytochalasin D treatment to provoke a drastic change in the power law coefficient and to demonstrate the feasibility of the approach to capture rheological changes extremely fast and precisely. The method is easily adaptable to different indenter geometries and acquires viscoelastic data with high spatiotemporal resolution.

INTRODUCTION

Cell mechanics has become a major research field due to its relevance for many biological processes comprising cell adhesion, division, growth, locomotion, and its biomedical impact on tissue formation, embryogenesis, and tumorigenesis (1–9). Changes in cell elasticity have become an indicator for cytotoxicity, malignancy, and abnormalities. Strong correlation with various diseases were proposed comprising cancer, vascular diseases, cardiomyopathies, etc. (10–13). In this context, Otto et al. (14) introduced a diagnostic tool based on real-time deformability cytometry to categorize cells based on their elastic properties and enable mechanical phenotyping. It is therefore of great interest to understand how cells respond mechanically to (bio)chemical and physical stimuli (1,5,6). In the case of animal cells, the cell's mechanical response to deformation originates mainly from the plasma membrane firmly attached to a contractile actomyosin network composed of cross-linked actin filaments as well as motor proteins such as myosin II (7,15–17). Living cells are soft composite

materials that actively contract under consumption of chemical energy and exhibit both solidlike elastic and fluidlike viscous properties. In response to external stress cells show typical viscoelastic phenomena such as creep and stress relaxation (18–20). In contrast to polymers and other soft matter, however, living cells were found to exhibit a weak power law dependence of their viscoelastic moduli on frequency (21–24). This power law confirms the absence of discrete relaxation times in the system and is often interpreted in terms of soft glassy materials (25,26). While the biophysical interpretation of power law behavior is intricate, its existence simplifies data analysis tremendously because only a single parameter describes the energy dissipation associated with deformation. Experimental timescales can be rather narrow and still sufficient to extract the power law coefficient with high precision.

Experimental techniques suitable to probe mechanical properties of individual cells can be roughly classified into optical, magnetic, or mechanical methods. Highest force resolution is usually obtained with magnetic tweezers (fN-pN) followed by optical tweezers (pN-nN) and rounded off by atomic force microscopy (AFM; pN-μN), which also covers the largest force range (27–29). Numerous studies exist where conventional atomic force microscopy

---

CrossMark

was used to produce force distance curves subject to nonlinear fitting of classical contact models that give access to the Young's modulus of adherent cells (27,30–38). The main advantage of this approach is its versatility, as AFM can be used for imaging simultaneously to force transmission and force measurement (27,39). Spatiotemporal resolution is very high and tip geometry or chemistry can readily be altered to meet the demands of the sample (7). For instance, this technique can gather data quickly enough to capture motile cells and to exert mechanical stimuli over a wide force range (40). A multitude of both local and whole-cell studies can be performed on living cells in their native environments using a large portfolio of modes ranging from force distance curves to microrheological studies in which the oscillation frequency of the cantilever is changed (21,41–43). Commonly, Young's moduli obtained from indentation experiments with different indenter geometries range between 0.1 and hundreds of kPa depending on the cell type (27,44). Brain cells are among the softest and osteoblasts and chondrocytes among the stiffest. Cell stiffness is highly correlated with the thickness and number of attachment sites of the actomyosin cortex to the membrane, the amount of excess area stored in the plasma membrane, adhesion, and osmotic pressure (7,8,15,16). Severing actin filaments as well as arresting myosin motors can have a drastic effect on the estimated Young's moduli (7,8,34). Shroff et al. (45) were among the first to investigate the frequency-dependent viscoelastic properties of samples using a method that applies small-amplitude oscillations of the AFM cantilever in contact with the cell body. They were able to determine the apparent dynamic modulus, the ratio between applied force and sample indentation, of single cardiomyocytes during contraction. Mahaffy et al. (21) and Alcaraz et al. (41) worked out the theoretical and experimental details allowing us to cover a broad frequency range giving access to the quantitative viscoelastic properties of cells with a controlled nondestructive stress range (100 Pa–10 kPa). Lu et al. (46) investigated the viscoelastic properties of individual glial cells and neurons in the central nervous system finding that in all cells of the central nervous system, the elastic behavior dominates over the viscous behavior and that surprisingly glial cells are even softer than their neighboring neurons. Rother et al. (42) examined the correlation between malignancy of tumor cells with their rheological properties. Darling et al. (20) employed the elastic viscoelastic correspondence principle to describe stress relaxation experiments performed on chondrocytes. More recently Hecht et al. (47) introduced an AFM imaging technique for mapping the viscoelastic power law parameters with submicrometer resolution. The new AFM mode combines conventional force mapping with additional force-clamp phase during each force-distance curve. The creep behavior during the force-clamp phase is analyzed according to a weak power law providing both the Young's modulus and the power law coefficient.

Here, we introduce a more general approach to implement viscoelasticity in the analysis of conventional force distance curves by fitting the entire force cycle with an appropriate viscoelastic model. We show that this method is highly robust, fast, and precise. It does not require any change in experimental design, is compatible with findings from conventional microrheology, and captures the impact of actin disintegrating Cytochalasin D on the mechanical properties of cells.

MATERIALS AND METHODS

Cell culture

Madin-Darby canine kidney cells, strain II (MDCK II; Health Protection Agency, Salisbury, UK) were maintained in minimum essential medium with Earle's salts, 2.2 g/L NaHCO$_3$, 10% fetal bovine serum, and 4 mM L-glutamine in a humidified incubator set to 37°C and 5% CO$_2$. Cells were released using trypsin/EDTA (0.05%/0.02%) and subcultured three times per week. During experimentation, medium additionally contained penicillin (0.2 mg/ml), streptomycin (0.2 mg/mL), amphotericin B (0.5 mg/mL), and HEPES (15 μM). Cytochalasin D ready-made solution (Sigma-Aldrich, Steinheim, Germany) was diluted with cell culture medium to a concentration of 10 μM. Cells were incubated with drug-containing medium for 15 min at 37°C.

AFM

Force cycle experiments

Cells were grown in Petri dishes (μ-Dish; ibidi, Martinsried, Germany) for 2 days until confluence was reached. Force indentation curves were recorded using a JPK NanoWizard II or NanoWizard 3 AFM (JPK Instruments, Berlin, Germany) mounted on an inverse fluorescence microscope (IX 81; Olympus, Tokyo, Japan) equipped with a CCD-camera (XM 10) and a 40× objective (LUCPLFLN) (all from Olympus) and a PetriDish-Heater (JPK Instruments) to keep the cells at 37°C. Force indentation curves were only recorded in the center of the cell to reduce the variance. Pyramidal cantilevers (MLCT, k_{nom} = 0.01 pN/nm; Bruker AFM Probes, Camarillo) with a slight asymmetry (front angle 15°, side angle 17.5°, and back angle 25°) at a tilt of 11° or spherical probes (CP-PNPL-SiO-A, R = 1 μm, k_{nom} = 80 pN/nm; sQube, Bickenbach, Germany) were used. For simplicity, we chose an average angle of α = 17.5° in our calculations. The spring constant of each cantilever was determined before the experiment using the thermal noise method according to Hutter and Bechhoefer (48), refined by Butt et al. (39) and Butt and Jaschke (49). The calibration factor (inverted optical lever sensitivity) is obtained from a force curve recorded on a rigid substrate (Petri dish). The cantilever velocity was set to 2 μm/s and force curves were corrected by baseline correction. Data reduction was carried out with a self-written MATLAB script (The MathWorks, Natick, MA) that also allows fitting of the contact point. In most cases, however, we rely on a manual assignment of the contact point. A comprehensive overview of how to determine the contact point is given by Gavara (50).

Oscillatory microrheology

AFM active microrheology experiments were carried out as described in Rother et al. (43). In brief, a MFP-3D-BIO set-up equipped with a Bio-Heater (both Oxford Instruments Asylum Research, Santa Barbara, CA), mounted on an inverted light microscope (IX 51; Olympus) was used. Pyramidal cantilevers (MLCT, k_{nom} = 0.01 pN/nm; Bruker, Camarillo, CA) were used. All experiments were performed at 37°C. The spring

constant, the lever sensitivity, and the hydrodynamic drag force acting on the cantilever in different distances from the surface were determined before each experiment on a stiff glass substrate. After the system was well calibrated and thermally equilibrated, force maps of 32×32 force distance curves were collected (cantilever velocity: 3 μm/s; trigger point: 500 pN). The cantilever was held in this indented position for 0.5 s before starting an oscillation protocol with oscillation frequencies ranging from 5 to 100 Hz at small amplitudes ($A = 40$ nm, peak to peak). After another 0.5 s without oscillation, the cantilever was retracted from the cell. From the overall 1024 force-indentation curves, only those obtained from the center of the cell were chosen for further mechanical analysis to avoid artifacts from the stiffer cell boundaries. Force-distance curves showing mechanical instabilities or artifacts were disregarded as well. A power law structural damping model was fit to the averaged storage (G') and loss modulus (G'') providing the fit parameters for the power law coefficient β and the scaling factor of stiffness G_0.

F-actin staining and confocal laser scanning microscopy

Cells were grown to confluence on Petri dishes (μ-Dish; ibidi, Martinsried, Germany), manipulated as desired and fixed afterwards by incubation with paraformaldehyde solution (4% (weight/volume) in phosphate buffered saline without calcium and magnesium (PBS^{--})) for 20 min. To permeabilize the cellular plasma membrane and to block unspecific binding sites, cells were incubated with blocking buffer (5% (weight/volume) bovine serum albumin, 0.3% (volume/volume) Triton X-100 in PBS^{--}) for 30 min. F-actin labeling was performed using AlexaFluor 488- or AlexaFluor 546-phalloidin (Life Technologies, Carlsbad, CA), diluted with PBS^{--} to a concentration of 165 nM. The cells were incubated at room temperature for 45 min. Cell nuclei were labeled with 4′,6-diamino-2-phenylindole (Life Technologies), diluted to a concentration of 50 ng/mL. Incubation time: 15 min at room temperature. Between every labeling step, cells were rinsed three times with PBS^{--} for 5 min each on a vibratory plate (75 rpm). Fluorescence imaging was performed using a confocal laser scanning microscope (FluoView1200; Olympus) equipped with a $100\times$ oil immersion objective (UPLFLN100×O2PH, NA = 1.3; Olympus).

Theory

Elastic contact

A widely accepted way to quantify the elasticity of cells from force indentation curves measured with an AFM is using Hertz's theory of elastic contacts to model the data (51–53). Although contact mechanics based on Hertz's theory is strictly valid only if the indentation depth is <10% of the sample thickness, which in the case of cells is often not more than a few hundreds of nanometers, the model is very popular because the experiment is condensed to a single parameter, the so-called Young's modulus (30,54). The Hertz model also requires that the material is an isotropic and fully elastic continuum (51–53), which might not be the case for all cell types (7,17). Depending on the indenter geometry different functions how the force depends on the indentation depth are obtained. For instance, the force-indentation relationship for a conical punch indenting an elastic half-space is given as (55):

$$f = \frac{2E \tan \alpha}{\pi(1 - \nu^2)} h^2, \tag{1}$$

while for a spherical indenter one obtains the well-known Hertz solution (51):

$$f = \frac{4E\sqrt{R}}{3(1 - \nu^2)} h^{\frac{3}{2}}. \tag{2}$$

For a cylindrical flat punch with constant contact area the relationship between force and indentation depth is linear (56):

$$f = \frac{2a_{cp}E}{1 - \nu^2} h, \tag{3}$$

where f is the force response of the cantilever, h is the indentation depth, R is the radius of the spherical probe, a_{cp} is the radius of the flat cylindrical punch, and α is the half opening angle of the conical indenter. The values E and ν are the Young's modulus and Poisson's ratio of the material that is being indented, respectively. While the validity of these solutions of the contact problem in the absence of adhesion is limited to elastic solids, they are nonetheless routinely applied to elastic-plastic indentations by assuming that the initial unloading segment of the load-displacement curve is linearly elastic. In an elastic indentation, where the loading and unloading curves follow the same path, Eqs. 1–3 and subsequent derivations are valid at all h.

Cells, however, possess both viscous and elastic properties in varying degrees (57). For any viscoelastic material, internal stresses are a function not only of the instantaneous deformation, but also depend on the history of deformation (58). Surely, the most recent history has the highest impact. Linear viscoelasticity is the simplest possible description of any viscoelastic material. If a material is subject to deformations or stresses so small that its rheological response functions are independent of strain or stress, the response is in the linear viscoelasticity regime (58). As far as AFM experiments are concerned, Darling et al. (20) were among the first to employ the elastic-viscoelastic correspondence principle to investigate the viscoelastic behavior of chondrocytes. Peng et al. (59) address the contribution of plastic deformation using a three-step loading profile in which viscoelastic contributions are present mainly in the holding segment. This procedure allowed the authors to study plastic and viscoelastic deformations separately and eventually permits us to determine the shear creep compliance of linear viscoelastic-plastic solids. Recently, Chyasnavichyus et al. (60) used a Johnson-modified Sneddon (55) approach in a combination with the standard linear solid model to describe the viscoelastic behavior of polymers. Because appropriate models to describe the situation of unloading correctly, i.e., where the contact radius decreases, are cumbersome and often require numerical solutions, most researchers use the method of Oliver and Pharr (61) that allows the evaluation of mechanical properties by concentrating on the earliest stages of the unloading curve, where the restoring material behavior is assumed to be purely elastic and the contact area not yet decreasing.

The following section briefly reviews how viscoelasticity can be integrated into common contact models extending the parameter space and correcting the elastic moduli that are now a function of loading history.

Viscoelastic contact

The relation between an increasing loading force $f(t)$ of a rigid indenter that is penetrating a linear viscoelastic body and the corresponding indentation depth $h(t)$ was first derived by Lee and Radok (62) for spherical indenters. The hereditary integrals are only valid if the contact area increases monotonically with time, i.e., in the time interval $0 < t < t_m$, in which t_m is the time corresponding to maximal contact radius $a(t_m) = a_{max}$. Generally, we obtain for the indentation depth $h(t)$ as long as $0 < t < t_m$:

$$h^n(t) = \tilde{C} \int_0^t J(t - \tau) \frac{df(\tau)}{d\tau} d\tau \tag{4}$$

or conversely (through $d\sigma = (E(t - \tau)/(1 - \nu^2))d\gamma$) for the force $f(t)$:

$$f(t) = \tilde{C}^{-1} \int_0^t E(t - \tau) \frac{dh(\tau)^n}{d\tau} d\tau, \tag{5}$$

with $J(t) = J_0\phi(t)$ the creep function and $E(t) = E_0\psi(t)$ the corresponding relaxation function connected via the Laplace transform ($\overline{\psi}(s)\overline{\phi}(s) = s^{-2}$, with s the Laplace variable). $\phi(t)$ and $\psi(t)$ are the normalized creep and relaxation functions, respectively. For a conical indenter geometry, we have $h(t) = (\pi/2)a(t)\cot\alpha$, $\tilde{C} = \tilde{C}_c = (\pi(1 - \nu^2)/(2\tan\alpha))$, and $n = 2$ (55). A four-sided pyramidal indenter requires a slightly different geometrical prefactor $\tilde{C}_c = (1.342(1 - \nu^2)/\tan\alpha)$ (47,63). For a spherical indenter we find $h(t) = (a^2(t)/R)$, $\tilde{C} = \tilde{C}_s = (3(1 - \nu^2)/(4\sqrt{R}))$, and $n = 3/2$ (51), while for a flat cylindrical punch the contact radius does not depend on indentation depth and therefore we can simply write $\tilde{C} = \tilde{C}_{cp} = (1 - \nu^2/(2a_{cp}))$ and $n = 1$ (52,56). Note that, surprisingly, the elastic solutions for $h(a(t))$ remain valid if $t < t_m$. A more general treatment has been suggested by Popov relating the contact radius to indentation depth for any shape of the axisymmetric indenter with shape function $s(r)$ (64):

$$h(t) = a(t)\int_0^{a(t)} \frac{s'(r)\mathrm{d}r}{\sqrt{a^2(t) - r^2}}, \qquad (6)$$

and for the force:

$$f(t) = 2E_0\int_0^t \psi(t - \tau)\frac{\partial}{\partial\tau}\left(\int_0^{a(\tau)} \frac{s'(r)r^2\mathrm{d}r}{\sqrt{a^2(\tau) - r^2}}\right)\mathrm{d}\tau. \quad (7)$$

The hereditary integrals can be solved for any loading conditions, such as creep at fixed load after a step load, linear ramping of force (constant velocity), or indentation at constant loading rate, and creep after monotonically increasing ramp loading as long as the contact radius is nondecreasing (58). However, this excludes analysis of the retraction curve in AFM experiments. Fortunately, Graham (65) and Ting (66) proposed a general solution to the problem, which will be also adapted here to describe the full force cycle.

In AFM experiments, ramps in $h(t) = \nu_0 t$ with constant velocity ν_0 are usually prescribed and the force response $f(h)$ is measured. We will first derive the theoretical force-indentation curve assuming a monotonically increasing contact radius. In the second section, we provide an analytical solution for the unloading case, for which $h(t) = \nu_0(2t_m - t)$ pertains.

Studies using a variety of techniques have shown that the rheological properties of cells are best captured by a power law creep function $\phi = (t/t_0)^\beta$ with $0 \leq \beta \leq 1$. The dimensionless power law coefficient β characterizes the degree of fluidity and energy dissipation upon deformation, where $\beta = 0$ represents an ideal elastic solid and $\beta = 1$ a Newtonian liquid. For cells, β is often found to be in the range of 0.2–0.3 indicative of a viscoelastic solid (23,42). Accordingly, the relaxation function is $\psi = (t/t_0)^{-\beta}$ with the timescaling parameter t_0. Note that due to $\overline{E}(s)\overline{J}(s) = 1/s^2$ we have in the time domain $E(t) = (1/(J_0\Gamma(1 + \beta)\Gamma(1 - \beta)))(t/t_0)^\beta$. The power law prefactor $E_0 = (1/(J_0\Gamma(1 + \beta)\Gamma(1 - \beta)))$ is a measure of the cell's stiffness at the time $t = t_0$. Because E_0 and t_0 are not independent due to the scaling invariance of the power law, the timescaling parameter t_0 can be chosen arbitrarily and is usually set to $t_0 = 1$ s (47). Therefore E_0, the scaling parameter for the cell's modulus, is the apparent Young's modulus at a timescale of 1 s and might deviate from Young's moduli obtained from elastic models that are time-independent. In the remainder of the text, we will explicitly work with these power law creep and relaxation functions to derive an analytical expression for loading and unloading conditions describing the viscoelastic behavior of cells subject to indentation. In general, any other conceivable expression for $J(t)$ and $E(t)$ such as those from standard linear mechanical models can also be used.

Indentation curve—linear ramp with increasing $h(t)$. Assuming a conical or pyramidal indenter that penetrates the cell with a constant rate $h(t) = \nu_0 t$, we obtain for the force as a function of time as long as $0 < t < t_m$:

$$
\begin{aligned}
f(t) &= \frac{\nu_0^2}{\tilde{C}_c}\int_0^t E_0\left(\frac{t - \tau}{t_0}\right)^{-\beta}\tau\mathrm{d}\tau = \frac{\nu_0^2 E_0 t_0^\beta}{\tilde{C}_c(2 - 3\beta + \beta^2)}t^{2-\beta} \\
&= \frac{E(t)}{\tilde{C}_c(2 - 3\beta + \beta^2)}h^2(t).
\end{aligned}
$$
$$(8)$$

For a spherical indenter, we find:

$$
\begin{aligned}
f(t) &= \frac{\nu_0^{3/2}}{\tilde{C}_s}\int_0^t E_0\left(\frac{t - \tau}{t_0}\right)^{-\beta}\tau^{\frac{1}{2}}\mathrm{d}\tau \\
&= \frac{\nu_0^{3/2}E_0 t_0^\beta 3\sqrt{\pi}\Gamma(1 - \beta)}{\tilde{C}_s 4\Gamma\left(\frac{5}{2} - \beta\right)}t^{(3/2)-\beta} \\
&= \frac{3E(t)\sqrt{\pi}\Gamma(1 - \beta)}{\tilde{C}_s 4\Gamma\left(\frac{5}{2} - \beta\right)}h^{3/2}(t),
\end{aligned}
$$
$$(9)$$

with the gamma function $\Gamma(t) = \int_0^\infty x^{t-1}e^{-x}\mathrm{d}x$.

For a flat cylindrical punch, the force indentation curve is linear:

$$
\begin{aligned}
f(t) &= \frac{\nu_0}{\tilde{C}_{cp}}\int_0^t E_0\left(\frac{t - \tau}{t_0}\right)^{-\beta}\mathrm{d}\tau = \frac{\nu_0 E_0 t_0^\beta}{\tilde{C}_{cp}(1 - \beta)}t^{1-\beta} \\
&= \frac{E(t)}{\tilde{C}_{cp}(1 - \beta)}h(t).
\end{aligned}
$$
$$(10)$$

Note that, in AFM experiments, one usually has control only over the z-piezo movement and the assumption of a linear ramp of $h(t)$ has to be verified carefully. In Appendix A, we show that the assumption holds well for stiff cantilevers compared to the Young's modulus of the cells.

Retraction curve—linear ramp with decreasing $a(t)$. While indentation of a viscoelastic material with monotonically increasing contact area does not change the relation between contact radius and indentation depth, as it is known from the elastic case following Eq. 6, the situation becomes more intricate for a decreasing contact radius. In their seminal articles, Graham (65) and Ting (66) have devised a theory that permits to compute force, indentation, and contact area for arbitrary $a(t)$. The key step is, however, to find the time $t_1 < t_m$ at which $a(t) = a(t_1)$ for $t > t_m$, which might involve numerical integration and differentiation. In 2010, Greenwood (67) proposed a straightforward method of analysis by superposition of an assembly of viscoelastic punch indentations avoiding some of the involved mathematics connected with the approach of Ting (66). The method of Greenwood (67) leads to a more convenient form to describe the unloading case. In our case, due to the simplified creep and relaxation functions, we can find an analytical expression for $t_1(t)$ based on Ting's original article (66) that in turn enables us to compute the force acting on the cantilever in the same fashion as before:

$$f_b(t) = 2E_0\int_0^{t_1(t)} \psi(t - \tau)\frac{\partial}{\partial\tau}\left(\int_0^{a(\tau)} \frac{s'(r)r^2\mathrm{d}r}{\sqrt{a^2(\tau) - r^2}}\right)\mathrm{d}\tau. \quad (11)$$

In most AFM experiments the indentation is prescribed and the load force on the cantilever measured. Typically, linearly increasing ramps of $h(t)$ up to $t = t_m$ are applied and unloading occurs with the same rate until $h(t) = 0$ is reached again, giving rise to force cycles (Fig. 1, *top panel*). For $2t_m > t > t_m$, the rate for retraction is therefore prescribed

as $h(t) = \nu_0(2t_m - t)$. Importantly, the linear ramp also leads to a maximal contact radius at $t = t_m$ and therefore, the contact radius decreases monotonically if $t > t_m$. The value t_1 is obtained from the condition (66)

$$\int_{t_1(t)}^{t} \psi(t - \tau) \frac{\partial h(\tau)}{\partial \tau} \mathrm{d}\tau = 0, \tag{12}$$

leading to

$$\int_{t_1(t)}^{t_m} \psi(t - \tau) \frac{\partial \nu_0 \tau}{\partial \tau} \mathrm{d}\tau = \int_{t_m}^{t} \psi(t - \tau) \frac{\partial \nu_0(2t_m - \tau)}{\partial \tau} \mathrm{d}\tau. \tag{13}$$

Solving the integrals for $\psi(t) = (t/t_0)^{-\beta}$ provides $t_1(t)$:

$$t_1(t) = t - 2^{\frac{1}{1+\beta}} \left((-t_m + t)^{1+\beta} \right)^{\frac{1}{1+\beta}}. \tag{14}$$

For a conical indenter, the force f_b upon retraction is therefore:

$$f_b = \tilde{C}_c^{-1} \nu_0^2 \int_0^{t_1(t)} E_0 \left(\frac{t - \tau}{t_0} \right)^{-\beta} \tau \mathrm{d}\tau. \tag{15}$$

Together with Eq. 14, the integral can be solved analytically:

$$f_b(t) = \frac{\nu_0^2 E_0 t_0^\beta}{\tilde{C}_c} \left(\frac{2t^{2-\beta}}{\beta^2 - 3\beta + 2} + \frac{2^{\frac{1}{1-\beta}}(1-\beta)2\left((t - t_m)^{1-\beta} \right)^{\frac{1}{1-\beta}} + (\beta - 2)t}{(1-\beta)(2-\beta)\left(2^{\frac{1}{1-\beta}} \left((t - t_m)^{1-\beta} \right)^{\frac{1}{1-\beta}} \right)^{\beta - 1}} \right). \tag{16}$$

Fig. 1 illustrates how the viscoelasticity of the sample changes the time dependency of the contact radius of a conical indenter and the corresponding load response if a linear indentation ramp is applied. Note that only in the advancing phase is the relation between indentation and contact radius solely given by the indenter shape—a surprising finding (66). Later, upon retraction the contact radius also depends on the material properties. The panel at the top shows the prescribed indentation ramp, the center panel the change in contact radius for two different values of β (*continuous line*, $\beta = 0.3$; *dotted line*, $\beta = 0.1$), and the plot at the bottom shows the corresponding force response (load) ($f \tilde{C}/(\nu_0^2 E_0 t_0^\beta)$) for a conical indenter. The green curve represents Sneddon's solution (55) in the absence of viscous losses with no hysteresis (energy dissipation) between approach and retraction. The receding contact area drops quicker to zero in the case of larger values for β because the highly viscous material does not follow the retracting indenter on its way from the surface to its initial position. The viscous contribution increases the relaxation time and therefore keeps the material from immediately adopting a given shape. The more elastic the material is, the more symmetric increasing and decreasing $a(t)$ becomes. Consequently, an increasing β generates a larger hysteresis between approach and retraction in the load (force) curve. Upon retraction, the force immediately drops due to the memory kernel in the viscoelastic

Eq. 15, i.e., the material's response is delayed compared to the movement of the indenter. Fig. 2 *A* illustrates the impact of β on the energy dissipation (hysteresis) visible in force cycle measurements (same parameters as in Fig. 1). Notably, the apparent stiffness also increases with higher values of β, although E_0 is constant because the overall resistance to indentation comprises elastic and viscous contributions. Therefore, neglecting energy dissipation leads to a systematic overestimation of cell stiffness. Fig. 2 *B* shows a fit of Eqs. 8 and 16 to experimental data obtained on a single MDCK II cell of a confluent monolayer.

Generally, the applicability of this approach relies on the assumption that the indentation as a function of time is precisely known. However, in conventional AFM experiments the only control variable is the z-piezo, and a linear ramp in $h(t)$ can only be ensured for stiff cantilevers compared with the stiffness of the sample and for low velocities. For cell experiments with sufficiently stiff cantilevers compared to the cell's Young's modulus and low indentation depth, this condition is usually fulfilled (see Appendix A).

RESULTS AND DISCUSSION

As a test bed for our viscoelastic description of adherent cells, we chose to examine the viscoelastic properties of confluent MDCK II cells cultured on petri dishes. The elastic and viscoelastic properties of this cell line have been thoroughly investigated in the past (7,8,30). To study changes of the power law coefficient β, we treated the cells with Cytochalasin D, which disintegrates the actin cortex and is known to increase β considerably but at the same time softens the cells. Our results from fitting both approach and retraction curves are directly compared with other established methods such as AFM-based microrheology using the same cells and cantilevers. In addition, we varied the indentation depth and indenter geometry (Figs. S1–S5; Table S1) to examine the influence of nonlinear contributions and to determine the validity and robustness of our approach, i.e., fitting the full force cycle using Eq. 8 for the indentation ($t \leq t_m$) and Eq. 16 for retraction ($t > t_m$) away from the cell.

Fig. 3 *A* (*left*) shows microrheological data (G', G'') obtained from a confluent MDCK II monolayer subject to an oscillating pyramidal indenter placed at a given maximal restoring force (500 pN) and excited to a peak-to-peak amplitude of ~40 nm at each frequency (5–100 Hz). The force $f(\omega)$ is measured as a function of frequency and the
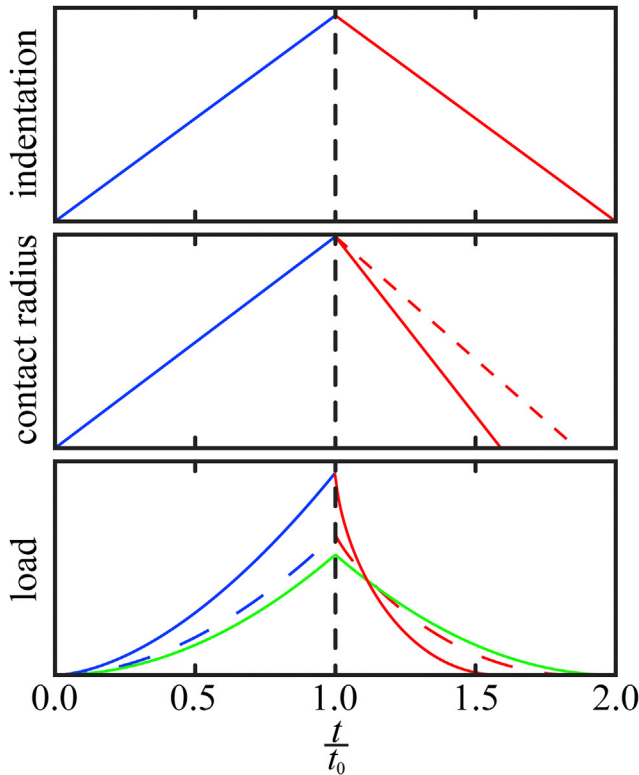
FIGURE 1 Impact of applying a linear indentation ramp (*top*) of a conical indenter up to $t_m = 1$ s (*vertical black line*) on the contact radius (*center*) and on the response (dimensionless load) of the cantilever (*bottom*). The blue traces describe the approach until the maximal indentation depth is reached, and the red traces describe the retraction. Two different values for β ($\beta = 0.3$: *continuous lines*; $\beta = 0.1$: *dashed lines*) were used to illustrate the effect of viscoelasticity on the force response. For comparison, the purely elastic case is shown in green ($\beta = 0$). To see this figure in color, go online.

following expression for the complex shear modulus G^* is obtained (41):

$$G^*(\omega) = G' + iG'' = \frac{1-\nu}{3h_0\tan\alpha}\left(\frac{f(\omega)}{h(\omega)} - i\omega b(h_0)\right), \quad (17)$$

where $b(h_0)$ is the drag coefficient at an extrapolated tip-surface in direct contact and ω is the angular frequency in radians per second. Many microrheological measurements performed on tens of different cells are compiled in Fig. 3 *A*. G^* increases with frequency following a weak power law with an exponent β of ~0.27 (Fig. 3 *A*), while G'' exhibits lower values than G' in the low-frequency regime (<50 Hz). In this regime, the cells behave more like an elastic solid as the loss tangent ($\eta = G''/G'$) stays <1. At larger frequencies, cells adopt more fluidlike properties. An attempt to explain this power law behavior in the microrheological spectra of living cells has been suggested by Kollmannsberger and Fabry (23,26). By describing the cell as an active soft glassy material, some rheological features can be assigned to cytoskeletal organization and remodeling. This is based on the soft glassy rheology model first described by Sollich (25) and assumes that the cytoskeleton of the cell consists of many disordered elements, which are held together by weak attractive forces between neighboring elements trapping the elements in energy wells (25,26). These weak interactions allow the elements to occasionally jump between the potential wells. A large distribution of energy-well depths leads to a scale-free (power law) behavior of the lifetime distribution and thus results in a power law rheological behavior (26). The obtained frequency-dependent data of the complex shear modulus G^* were fitted with the power law structural damping (Eq. 18) using a complex nonlinear least-squares fitting routine:

$$G^* = G_0\Gamma(1-\beta)\cos\left(\frac{\pi}{2}\beta\right)\left(1 + i\tan\left(\frac{\beta\pi}{2}\right)\right)\left(\frac{\omega}{\omega_0}\right)^\beta$$
$$+ i\omega\mu, \quad (18)$$

with G_0 as the scaling factor describing the stiffness of the sample, β as the same power law coefficient as used in the time domain, ω_0 as the scaling factor of the frequency (set to 1 rad/s), and μ is the viscosity. G_0 can be easily converted
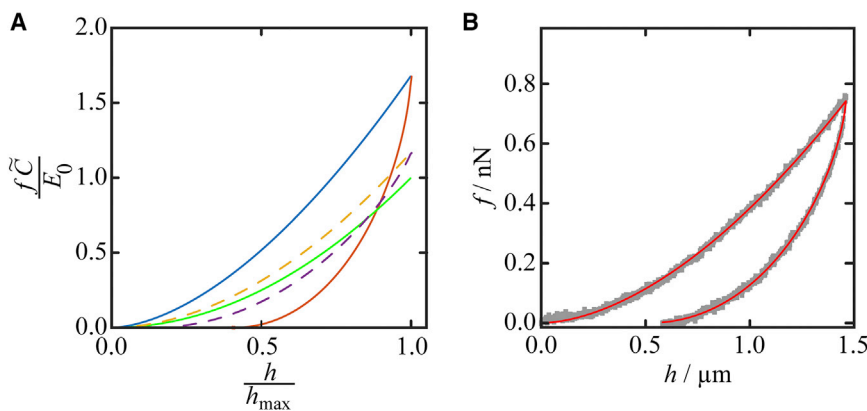

FIGURE 2 (*A*) Normalized load as a function of normalized indentation depth corresponding to the time-dependent loading and unloading shown in Fig. 1 employing Eqs. 8 and 16. Two different values for β ($\beta = 0.3$: *continuous lines*; $\beta = 0.1$: *dashed lines*) were used to illustrate the effect of viscoelasticity on the force response ($v_0 = 1$ μm/s). For comparison, the purely elastic case (Eq. 1) is shown in green ($\beta = 0$). (*B*) Nonlinear fit (*red line*, $\beta = 0.263 \pm 0.002$, $E_0 = (764 \pm 4)$ Pa) according to Eqs. 8 and 16 to force-cycle data (*gray dots*) obtained from indentation of a single MDCK II cell with a pyramidal indenter at $v_0 = 2$ μm/s. To see this figure in color, go online.
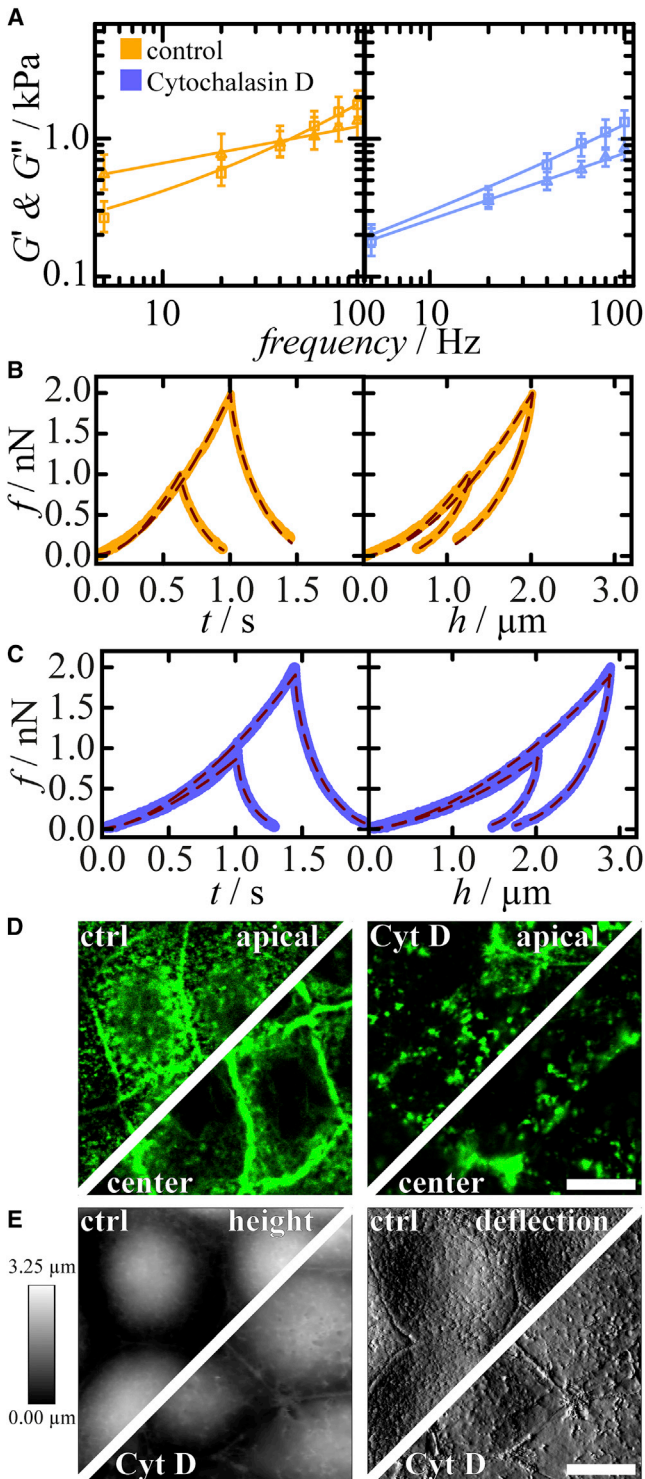
FIGURE 3 (A–C) Rheological information obtained from force measurements performed on confluent MDCK II cells. (A) Microrheology data obtained from forced oscillatory experiments. Storage (G′, triangles) and loss (G″, squares) moduli are shown in a frequency regime between 5 and 100 Hz; (solid lines) power-law structural damping fit (Eq. 18) to the data. (B and C) Representative force curves of either untreated cells (orange, B) or Cytochalasin D-treated cells (15 min, 10 μM, blue, C) using a pyramidal indenter. (Left) Force response during indentation-retraction experiments over time used to fit the model to the data. (Right) Force response

in the apparent Young's modulus E_0 by $E_0 = 2G_0(1 + \nu)$, where ν is Poisson's ratio, which we set to 0.5 as incompressibility is typical for soft biological matter (47). On the right-hand side of Fig. 3 A, viscoelastic spectra of cells treated with Cytochalasin D for 15 min are shown. It becomes immediately clear that cells soften considerably after administration of Cytochalasin D because both G' and G'' decrease and the cells adopt more liquidlike mechanical properties as the loss tangent is >1 in the full frequency range. Moreover, the power law coefficient β, which is a good indicator for this transition from an elastic solid to a viscous liquid, is close to 0.5 after incubation with Cytochalasin D. Note that for $\beta \rightarrow 1$, cells would behave like a Newtonian liquid, while for an elastic solid, $\beta = 0$ holds. The reason for this fluidization is loss of the actomyosin integrity because Cytochalasin D inhibits actin polymerization and therefore leads to disintegration of the F-actin cytoskeleton. Consequently, cells soften, become more roundish, loosen cell-cell contacts, and then eventually detach from the surface. The loss of network elasticity reduces the elastic contributions and the cells behave like a liquid droplet surrounded by a membrane.

Fig. 3 B shows typical force cycle experiments (approach and retraction, orange lines) as a function of time ($f(t)$, left) and as a function of indentation depth ($f(h)$, right) using a pyramidal indenter approaching with a linear ramp at a constant velocity of 2 μm/s. The direction of the movement was immediately reversed with the same velocity at $t = t_m$, the time where the maximum indentation depth is reached. The obtained $f(t)$ curves were subject to fitting using Eq. 8 for $t \leq t_m$ and Eq. 16 if $t > t_m$. The corresponding indentation depth was later computed from $h(t) = v_0 t$ if $0 < t \leq t_m$ and $h(t) = v_0(2t_m - t)$ for $t > t_m$, giving rise to the panels on the right-hand side of Fig. 3 B. Fits are shown as dashed dark-red lines. Fig. 3 C shows the impact of Cytochalasin D on the force distance curve (thick blue lines). Cells become softer because the slope of the approach curve becomes smaller resulting in lower E_0 and the hysteresis becomes more pronounced indicative of a larger power law coefficient β.

Fig. 4 compiles the results obtained from AFM-based oscillatory microrheology (OMR) and force cycle experiments

as a function of indentation depth $h(t)$. Two different indentation depths are shown exemplarily. (Dashed lines) The corresponding fits of Eqs. 8 and 16. For untreated cells, we obtain for the force cycle with low maximal force: $E_0 = (1633 \pm 26)$ Pa, $\beta = 0.183 \pm 0.006$, and for high maximal force: $E_0 = (1258 \pm 9)$ Pa, $\beta = 0.233 \pm 0.003$, respectively. For Cytochalasin D-treated cells we obtain for low maximal force: $E_0 = (354 \pm 3)$ Pa, $\beta = 0.436 \pm 0.003$, and for high maximal force: $E_0 = (496 \pm 2)$ Pa, $\beta = 0.373 \pm 0.002$, respectively. (D) Confocal fluorescence images of AlexaFluor488-Phalloidin F-actin-labeled MDCK II cells before and after Cytochalasin D treatment (15 min, 10 μM). (E) AFM height (left) and deflection (right) images of MDCK II cells before and after Cytochalasin D treatment (15 min, 10 μM). (D and E) Scale bar, 10 μm. To see this figure in color, go online.
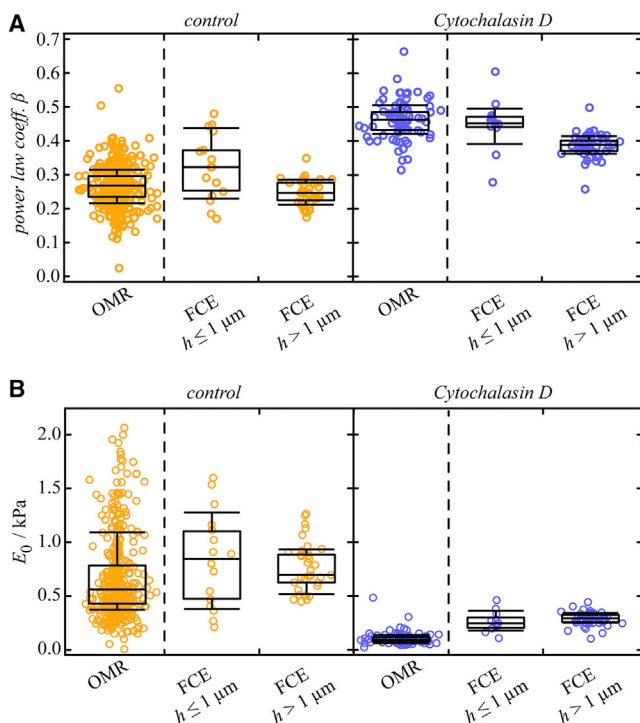
FIGURE 4 Viscoelastic properties of confluent MDCK II cells measured by different techniques. (*A*) Power law coefficients and (*B*) Young's moduli E_0 obtained from different experimental methods (OMR and FCE), cell treatments (*orange*, control cells; *blue*, after Cytochalasin D incubation with 2–10 μM, 15 min), and variable indentation depths. To see this figure in color, go online.

(FCE) in the absence and presence of Cytochalasin D. In the case of force cycle experiments the data is classified into low indentation depth ($h_0 \leq 1\ \mu$m) and high indentation depth ($h_0 > 1\ \mu$m). The actual values of indentation depth at a given force are shown in Fig. S6 (Supporting Material). Oscillatory microrheological experiments of untreated confluent MDCK II cells provide a narrow distribution of power law coefficients centered at $\beta = 0.268 \pm 0.003$ (median $\pm$ SEM). Force cycle experiments performed with a pyramidal indenter on the same cells up to indentation depths of $h_0 \leq 1\ \mu$m, led to $\beta = 0.32 \pm 0.02$. Deeper indentation ($h_0 > 1\ \mu$m) leads to slightly smaller values of $\beta = 0.25 \pm 0.01$. Already at visual inspection of a series of force cycle measurements with increasing maximal force, it becomes clear that indentation depth has only a minor impact on the rheological parameters (Fig. S7). Essentially, we found that the power law coefficient measured by OMR can be reproduced using full force cycle fits using Eqs. 8 and 16. The value for β only slightly depends on the maximum indentation depth h_0 leading to smaller values for β if $h_0 > 1\ \mu$m (Fig. 4 *A*). Using a small spherical indenter and modifying Eqs. 8 and 16 accordingly, we obtain essentially identical β-values (Fig. S5). Therefore, we conclude that β is robust against indentation depth and indenter geometry.

Treatment of confluent MDCK II cells with actin disintegrating Cytochalasin D leads to a substantial increase of the power law coefficient compared to that found for control cells regardless of the type of rheological measurement (FCE or OMR). Force cycle experiments up to indentation depths of 1 μm result in $\beta = 0.45 \pm 0.02$ or $\beta = 0.39 \pm 0.01$ if $h_0 > 1\ \mu$m, respectively. Using OMR, we obtain a median value of $\beta = 0.46 \pm 0.01$.

Generally, we found that E_0 values determined by OMR and FCS are also in very good agreement. We found an average apparent Young's modulus of $E_0 = (0.8 \pm 0.1)$ kPa ($h_0 \leq 1\ \mu$m) and $E_0 = (0.70 \pm 0.04)$ kPa ($h_0 > 1\ \mu$m) using FCE, while OMR provides slightly smaller values of $E_0 = (0.57 \pm 0.05)$ kPa, however, with a skewed distribution toward larger E_0 values (Fig. 4).

After incubation with Cytochalasin D for 15 min, E_0 drops to $E_0 = (100 \pm 7)$ Pa in OMR measurements and to $E_0 = (247 \pm 29)$ Pa in FCE if $h_0 \leq 1\ \mu$m and $E_0 = (296 \pm 9)$ Pa if $h_0 > 1\ \mu$m.

The fits according to Eqs. 8 and 16 describe the experimental data usually very well, especially if the prestress is not too high (Fig. 2). In some curves, however, deviations from the model are observed at low indentation depth (Fig. S8). These deviations are attributed to substantial cortical tension giving rise to a prestress, as a consequence of actomyosin contractility. This could, in principle, easily be accounted for by adding a linear term to the force as a function of indentation depth (Fig. S8). However, here we refrain from adding a linear term without derivation from first principles because it has neither been used by others nor in our microrheological data evaluation and has only a small impact on the energy dissipation, i.e., the hysteresis between loading and unloading.

Compared with data found in literature, our measured values for β fall into the same range usually reported for adherent cells. Also, the treatment with Cytochalasin D liquidizes the exposed cells marked by an increase in β as reported by others using mainly OMR (21–24). Notably, using a spherical indenter (2 μm diameter) instead of the pyramidal indenter, identical values for β are obtained for confluent MDCK II cells (Fig. S5). The values found for the Young's modulus E_0 assuming essentially $\beta = 0$ are more widespread ranging from 400 Pa to several kPa for MDCK II cells (7,30,43). Compared with actual values provided by Harris and Charras (68) (400 Pa for wt MDCK and 147 Pa after Cytochalasin D treatment), our values obtained by FCE and OMR are in the same scope. Notably, cellular elasticity depends also on the culture conditions and passage number, a possible source of variance. The indenter geometry might also be important because contact models do not capture the shell-like structure of cells correctly (7), which might lead to an apparent geometry dependence of the Young's modulus (7). Interestingly, here the power law coefficient β was found to be indenter-geometry invariant (Fig. S5).

It is therefore important to recognize the general limitations of contact models in the context of describing cellular mechanics. First, the composite, shell-like structure of the

cell-cortex subject to deformation is not captured by contact models assuming that the cells can be treated as a semiinfinite viscoelastic continuum, where details of the structure are lumped into a single parameter, the Young's modulus. Second, surface structures (roughness) displayed by the cell, cortical tension, and area dilatation at large indentation depth are not explicitly considered by most contact models, albeit this might be fixed. Third, morphology and shape of the cells is usually heavily simplified because the cells were either considered to be planar or assumed to adapt the shape of a spherical cap. More complex geometries deviating from axisymmetry are typically ignored. Considering that at low indentation depth the indenter is sufficiently small compared with the cell, the effect of morphology is probably rather small. Despite the above-mentioned shortcomings of contact models based on Hertzian mechanics, these models have proven to be highly suitable to characterize the stiffness of the cells, especially if data from different laboratories are compared or cells are exposed to external stimuli such as cytoskeletal drugs. Here, our main goal was to provide an analytical function that permits us to obtain another independent parameter that reports on the energy dissipation associated with indentation experiments. The power law coefficient β turns out to be very robust against variation of indentation depth and indenter geometry. This way, cumbersome microrheological experiments can be substituted by force cycle experiments.

In summary, we derived analytical solutions for the viscoelastic contact of a conical indenter with adherent cells for increasing and decreasing contact radius. Therefore, both indentation and retraction can be described, giving access to the creep and relaxation function of cells. We found that the power law coefficient β is a robust parameter to classify the viscoelastic properties of cells independent of indentation depth, indenter geometry, and chosen micromechanical method. This might not be the case for a larger frequency range as pointed out by Stamenović et al. (69), but is valid for most experimental timescales (23,42). Because force cycle experiments are the standard way to measure elastic properties of cells or soft matter in general with an AFM, our approach to provide explicit analytical functions to describe both indentation and retraction curves not only permits us to determine the power law coefficient β but also provides quantitative values for the Young's moduli corrected for viscous effects (see Eq. 8). In comparison with the method of Hecht et al. (47), which also allows the mapping of the power law coefficient β on adherent cells based on force clamp after indentation, our approach is faster because no dwell time is needed and it is more robust against drift.

CONCLUSION

Broad consensus exists that the viscoelastic properties of cells can be described by power law creep and relaxation functions over a wide frequency range (10^{-2}–10^3 Hz) resulting from timescale-invariant processes reminiscent of soft glass rheology. Cells' frequency-dependent shear modulus is typically inferred either from deformation in response to an applied force or passively from the motion of associated tracer particles following the stochastic motion of a generalized Langevin equation. Although there might be a cell-specific transition of power laws at low and high frequency as predicted from microrheology of artificial networks, it is clear that a purely elastic description of cells can lead to a flawed interpretation. Elastic moduli are no longer constants but scale with the time and frequency of loading according to a single weak power law ($\beta \approx 0.2$). This implies that a single parameter, the power law coefficient, alters elastic moduli and captures the energy dissipation apparent in a hysteresis between approach and retraction of an indenter in force cycle experiments. The mechanical properties of adherent cells are conveniently probed with an AFM by raster scanning. Recording force distance curves at high spatial resolution—often termed "force volume measurement"—provides images based on material contrast. Although it is indisputable that cells are viscoelastic entities, this fact is usually ignored in AFM-based experiments and instead time-independent elastic moduli are used to describe the data. Our approach enlarges the parameter space of conventional AFM experiments comprising indentation and retraction by describing the full force cycle and thereby providing a corrected Young's modulus E_0 and the power law coefficient β. Proof-of-principle data is provided using the well-established cell line MDCK II subject to an actin disintegrating agent and comparison with AFM-based oscillatory microrheology. An analytical solution to the problem of indentation and unloading of cells with a conical indenter is provided, which can be easily adapted to other geometries and viscoelastic functions.

APPENDIX A: LINEAR INDENTATION RAMPS IN AFM EXPERIMENTS

An important prerequisite for this analysis of force cycle measurements in the time domain is the validity of the assumption that the indentation depth $h(t)$ changes with time in a linear fashion. Typically, in AFM experiments we only have control over the piezo movement and not the indentation depth. The following paragraph shows that the assumption $h(t) \approx v_0 t$ holds for stiff cantilevers compared to the stiffness of the sample.

Elastic solids

We know that the piezo movement is strictly prescribed to be linear in time ($z_p = v_0 t$) and the force measured by cantilever deflection $z_c = v_0 t - h$ is $f = k_c(v_0 t - h)$. Plugging the force acting on the cantilever, which is in equilibrium with the force experienced by the soft substrate, into the constitutive equation of a conical indenter we obtain:

$$f = k_c z_c = \frac{E_0}{\bar{C}_c} h^2. \tag{19}$$

Rearranging Eq. 19 gives:

$$h = \frac{\sqrt{1 + 4\frac{E_0}{\tilde{C}_c k_c}\nu_0 t} - 1}{2\frac{E_0}{\tilde{C}_c k_c}} \approx \frac{\frac{E_0}{\tilde{C}_c k_c}\nu_0 t - \left(\frac{E_0}{\tilde{C}_c k_c}\right)^2 (\nu_0 t)^2 + \mathcal{O}(\nu_0 t)^3}{\frac{E_0}{\tilde{C}_c k_c}}.$$

(20)

For $k_c \gg E_0$, the approximation $h \approx \nu_0 t$ holds for short times. Assuming a Young's modulus of $E_0 = 1000$ Pa for the cells, a spring constant of $k_c = 0.01$ N/m for the cantilever, and a nominal indentation depth of $h = 500$ nm, we arrive at a deviation at maximum indentation depth of $\approx 5\%$ compared to $z_p = \nu_0 t$. On the backside, however, this requires a sensitive measurement of z_c. This is warranted in most AFM experiments because nanometer changes in deflection are usually detected without difficulty. Fig. 5 shows the measured indentation depth h as a function of time, confirming that the assumption of a linear ramp together with decent sensitivity is fulfilled.

Soft glassy material

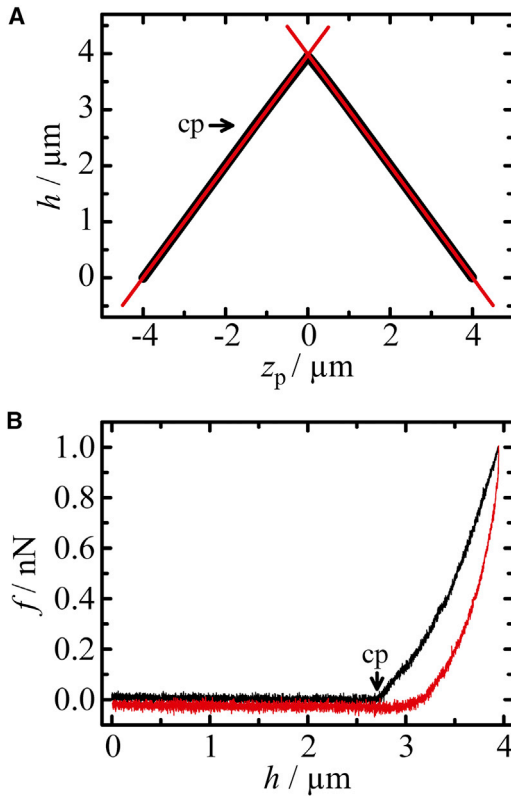In the case of cells indented with a cylindrical indenter (flat cylindrical punch), we obtain:

A

B

FIGURE 5 (A) Indentation depth h measured as a function of z-piezo movement z_p (*black dots*). The ramp is linear in time as indicated by the linear fits (shown in *red*). Velocity of piezo movement during approach and retraction was set to 2 μm/s and maintained at (1.99 ± 0.01) μm/s as inferred from fitting a straight line (*red line*). The label cp denotes the contact point with the surface. (B) Corresponding force distance curve (approach, *black curve*; retraction, *red curve*). To see this figure in color, go online.

$$h(t) = \frac{(1 - \nu^2)}{2a_{cp}} \int_0^t J_0 \left(\frac{t - \tau}{t_0}\right)^\beta \frac{\partial(k_c(\nu_0\tau - h(\tau)))}{\partial\tau} d\tau.$$

(21)

Note that we set $t_0 = 1$ s. Rewriting Eq. 21 gives:

$$h(t) = \tilde{C}_{cp}k_c\nu_0 \int_0^t J(t - \tau)d\tau - \tilde{C}_{cp}k_c \int_0^t J(t - \tau)\dot{h}(\tau)d\tau,$$

(22)

which, subject to Laplace transformation $\mathcal{L}\{\}$, simplifies to:

$$\overline{h}(s) = \tilde{C}_{cp}k_c\left(\nu_0\frac{\overline{J}(s)}{s} - \overline{J}(s)\overline{h}(s)s\right),$$

(23)

with $\mathcal{L}\{h(t)\} = \overline{h}(s)$, $\mathcal{L}\{\int_0^t J(u)du\} = \overline{J}(s)/s$, and the convolution $\mathcal{L}\{\int_0^t J(t - \tau)\dot{h}(\tau)d\tau\} = \overline{J}(s)\overline{h}(s)s$. Because the relation between creep function $J(t)$ and relaxation function $(E(t))$ in Laplace space is

$$\overline{E}(s)\overline{J}(s) = \frac{1}{s^2},$$

(24)

we obtain for $\overline{h}(s)$:

$$\overline{h}(s) = \frac{\frac{\nu_0}{s^2}}{\frac{\overline{E}(s)s}{\tilde{C}_{cp}k_c} + 1},$$

(25)

or as a geometric series:

$$\overline{h}(s) = \frac{\nu_0}{s^2}\left(1 - \frac{\overline{E}(s)s}{\tilde{C}_{cp}k_c} + \left(\frac{\overline{E}(s)s}{\tilde{C}_{cp}k_c}\right)^2 - \cdots\right).$$

(26)

Inverse Laplace transform $\mathcal{L}^{-1}\{\}$ of the truncated series (second term) gives:

$$h(t) = \nu_0 t + \nu_0 t \frac{E_0\beta}{\tilde{C}_{cp}k_c}\left(\frac{t}{t_0}\right)^{-(1+\beta)} = \nu_0 t + \frac{E_0\nu_0\beta}{\tilde{C}_{cp}k_c}\left(\frac{t}{t_0}\right)^{-\beta}.$$

(27)

Note that $\mathcal{L}^{-1}\{1/s^2\} = t$. For stiff cantilevers $k_c \gg E_0$ and low velocities, we can assume that $h(t)$ is linear in time. This means that for very high velocities and extremely soft cantilevers, the approximation might not hold. In cell experiments, we usually encounter Young's moduli of cells at ~100–1000 Pa, approaching velocities at ~1000 nm/s and spring constants of 0.01–0.1 N/m, rendering $h(t) \approx \nu_0 t$ a reasonable assumption.

SUPPORTING MATERIAL

Supporting Materials and Methods, eight figures, and one table are available at http://www.biophysj.org/biophysj/supplemental/S0006-3495(16)34338-7.

AUTHOR CONTRIBUTIONS

ACKNOWLEDGMENTS

REFERENCES

1. Fletcher, D. A., and R. D. Mullins. 2010. Cell mechanics and the cytoskeleton. *Nature.* 463:485–492.

2. Pollard, T. D., and G. G. Borisy. 2003. Cellular motility driven by assembly and disassembly of actin filaments. *Cell.* 112:453–465.

3. Pollard, T. D., and J. A. Cooper. 2009. Actin, a central player in cell shape and movement. *Science.* 326:1208–1212.

4. Stricker, J., T. Falzone, and M. L. Gardel. 2010. Mechanics of the F-actin cytoskeleton. *J. Biomech.* 43:9–14.

5. Hoffman, B. D., and J. C. Crocker. 2009. Cell mechanics: dissecting the physical responses of cells to force. *Annu. Rev. Biomed. Eng.* 11:259–288.

6. Janmey, P. A., and C. A. McCulloch. 2007. Cell mechanics: integrating cell responses to mechanical stimuli. *Annu. Rev. Biomed. Eng.* 9:1–34.

7. Pietuch, A., B. R. Brückner, …, A. Janshoff. 2013. Elastic properties of cells in the context of confluent cell monolayers: impact of tension and surface area regulation. *Soft Matter.* 9:11490–11502.

8. Pietuch, A., B. R. Brückner, and A. Janshoff. 2013. Membrane tension homeostasis of epithelial cells through surface area regulation in response to osmotic stress. *Biochim. Biophys. Acta.* 1833:712–722.

9. Pietuch, A., and A. Janshoff. 2013. Mechanics of spreading cells probed by atomic force microscopy. *Open Biol.* 3:130084.

10. Suresh, S. 2007. Biomechanics and biophysics of cancer cells. *Acta Biomater.* 3:413–438.

11. Affonce, D. A., and K. R. Lutchen. 2006. New perspectives on the mechanical basis for airway hyperreactivity and airway hypersensitivity in asthma. *J. Appl. Physiol.* 101:1710–1719.

12. Gimbrone, M. A., Jr., J. N. Topper, …, G. Garcia-Cardeña. 2000. Endothelial dysfunction, hemodynamic forces, and atherogenesis. *Ann. N. Y. Acad. Sci.* 902:230–240, discussion 239–240.

13. Lanzicher, T., V. Martinelli, …, O. Sbaizero. 2015. The cardiomyopathy lamin A/C D192G mutation disrupts whole-cell biomechanics in cardiomyocytes as measured by atomic force microscopy loading-unloading curve analysis. *Sci. Rep.* 5:13388.

14. Otto, O., P. Rosendahl, …, J. Guck. 2015. Real-time deformability cytometry: on-the-fly cell mechanical phenotyping. *Nat. Methods.* 12:199–202.

15. Brückner, B. R., A. Pietuch, …, A. Janshoff. 2015. Ezrin is a major regulator of membrane tension in epithelial cells. *Sci. Rep.* 5:14700.

16. Brückner, B. R., and A. Janshoff. 2015. Elastic properties of epithelial cells probed by atomic force microscopy. *Biochim. Biophys. Acta.* 1853:3075–3082.

17. Sen, S., S. Subramanian, and D. E. Discher. 2005. Indentation and adhesive probing of a cell membrane with AFM: theoretical model and experiments. *Biophys. J.* 89:3203–3213.

18. Pullarkat, P. A., P. A. Fernandez, and A. Ott. 2007. Rheological properties of the eukaryotic cell cytoskeleton. *Phys. Rep.* 449:29–53.

19. Desprat, N., A. Richert, …, A. Asnacios. 2005. Creep function of a single living cell. *Biophys. J.* 88:2224–2233.

20. Darling, E. M., S. Zauscher, and F. Guilak. 2006. Viscoelastic properties of zonal articular chondrocytes measured by atomic force microscopy. *Osteoarthritis Cartilage.* 14:571–579.

21. Mahaffy, R. E., C. K. Shih, …, J. Käs. 2000. Scanning probe-based frequency-dependent microrheology of polymer gels and biological cells. *Phys. Rev. Lett.* 85:880–883.

22. Fabry, B., G. N. Maksym, …, J. J. Fredberg. 2001. Scaling the microrheology of living cells. *Phys. Rev. Lett.* 87:148102.

23. Kollmannsberger, P., and B. Fabry. 2009. Active soft glassy rheology of adherent cells. *Soft Matter.* 5:1771–1774.

24. Kollmannsberger, P., C. T. Mierke, and B. Fabry. 2011. Nonlinear viscoelasticity of adherent cells is controlled by cytoskeletal tension. *Soft Matter.* 7:3127–3132.

25. Sollich, P. 1998. Rheological constitutive equation for a model of soft glassy materials. *Phys. Rev. E.* 58:738.

26. Kollmannsberger, P., and B. Fabry. 2011. Linear and nonlinear rheology of living cells. *Annu. Rev. Mater. Res.* 41:75–97.

27. Lim, C. T., E. H. Zhou, and S. T. Quek. 2006. Mechanical models for living cells—a review. *J. Biomech.* 39:195–216.

28. Neuman, K. C., and A. Nagy. 2008. Single-molecule force spectroscopy: optical tweezers, magnetic tweezers and atomic force microscopy. *Nat. Methods.* 5:491–505.

29. Haase, K., and A. E. Pelling. 2015. Investigating cell mechanics with atomic force microscopy. *J. R. Soc. Interface.* 12:20140970.

30. Hoh, J. H., and C. A. Schoenenberger. 1994. Surface morphology and mechanical properties of MDCK monolayers by atomic force microscopy. *J. Cell Sci.* 107:1105–1114.

31. Radmacher, M., M. Fritz, …, P. K. Hansma. 1996. Measuring the viscoelastic properties of human platelets with the atomic force microscope. *Biophys. J.* 70:556–567.

32. Lekka, M., P. Laidler, …, A. Z. Hrynkiewicz. 1999. Elasticity of normal and cancerous human bladder cells studied by scanning force microscopy. *Eur. Biophys. J.* 28:312–316.

33. Lekka, M., P. Laidler, …, A. Z. Hrynkiewicz. 2001. The effect of chitosan on stiffness and glycolytic activity of human bladder cells. *Biochim. Biophys. Acta.* 1540:127–136.

34. Rotsch, C., and M. Radmacher. 2000. Drug-induced changes of cytoskeletal structure and mechanics in fibroblasts: an atomic force microscopy study. *Biophys. J.* 78:520–535.

35. Sato, M., K. Nagayama, …, K. Hane. 2000. Local mechanical properties measured by atomic force microscopy for cultured bovine endothelial cells exposed to shear stress. *J. Biomech.* 33:127–135.

36. Steltenkamp, S., C. Rommel, …, A. Janshoff. 2006. Membrane stiffness of animal cells challenged by osmotic stress. *Small.* 2:1016–1020.

37. Guz, N., M. Dokukin, …, I. Sokolov. 2014. If cell mechanics can be described by elastic modulus: study of different models and probes used in indentation experiments. *Biophys. J.* 107:564–575.

38. Gavara, N., and R. S. Chadwick. 2012. Determination of the elastic moduli of thin samples and adherent cells using conical atomic force microscope tips. *Nat. Nanotechnol.* 7:733–736.

39. Butt, H.-J., B. Cappella, and M. Kappl. 2005. Force measurements with the atomic force microscope: technique, interpretation and applications. *Surf. Sci. Rep.* 59:1–152.

40. Schneider, D., T. Baronsky, …, A. Janshoff. 2013. Tension monitoring during epithelial-to-mesenchymal transition links the switch of phenotype to expression of moesin and cadherins in NMuMG cells. *PLoS One.* 8:e80068.

41. Alcaraz, J., L. Buscemi, …, D. Navajas. 2003. Microrheology of human lung epithelial cells measured by atomic force microscopy. *Biophys. J.* 84:2071–2079.

42. Rother, J., H. Nöding, …, A. Janshoff. 2014. Atomic force microscopy-based microrheology reveals significant differences in the viscoelastic response between malign and benign cell lines. *Open Biol.* 4:140046.

43. Rother, J., M. Büchsenschütz-Göbeler, …, A. Janshoff. 2015. Cytoskeleton remodelling of confluent epithelial cells cultured on porous substrates. *J. R. Soc. Interface.* 12:20141057.

44. Rodriguez, M. L., P. J. McGarry, and N. J. Sniadecki. 2013. Review on cell mechanics: experimental and modeling approaches. *Appl. Mech. Rev.* 65:060801–060841.

45. Shroff, S. G., D. R. Saner, and R. Lal. 1995. Dynamic micromechanical properties of cultured rat atrial myocytes measured by atomic force microscopy. *Am. J. Physiol.* 269:C286–C292.

46. Lu, Y.-B., K. Franze, …, A. Reichenbach. 2006. Viscoelastic properties of individual glial cells and neurons in the CNS. *Proc. Natl. Acad. Sci. USA.* 103:17759–17764.

47. Hecht, F. M., J. Rheinlaender, …, T. E. Schäffer. 2015. Imaging viscoelastic properties of live cells by AFM: power-law rheology on the nanoscale. *Soft Matter.* 11:4584–4591.

48. Hutter, J. L., and J. Bechhoefer. 1993. Calibration of atomic-force microscope tips. *Rev. Sci. Instrum.* 64:1868–1873.

49. Butt, H.-J., and M. Jaschke. 1995. Calculation of thermal noise in atomic force microscopy. *Nanotechnology.* 6:1–7.

50. Gavara, N. 2016. Combined strategies for optimal detection of the contact point in AFM force-indentation curves obtained on thin samples and adherent cells. *Sci. Rep.* 6:21267.

51. Hertz, H. R. 1882. On contact between elastic bodies. *J. Reine Angew. Math.* 94:156–171.

52. Johnson, K. L. 1985. Contact Mechanics. Cambridge University Press, Cambridge, UK.

53. Landau, L. D., and E. M. Lifshitz. 1986. Theory of Elasticity, Ed. 3. Butterworth-Heinemann, Oxford, UK.

54. Dimitriadis, E. K., F. Horkay, …, R. S. Chadwick. 2002. Determination of elastic moduli of thin layers of soft material using the atomic force microscope. *Biophys. J.* 82:2798–2810.

55. Sneddon, I. N. 1965. The relation between load and penetration in the axisymmetric Boussinesq problem for a punch of arbitrary profile. *Int. J. Eng. Sci.* 3:47–57.

56. Popov, V. L. 2010. Contact Mechanics and Friction: Physical Principles and Applications. Springer, Berlin, Germany.

57. Fung, Y. C. 1993. Biomechanics. Springer, New York.

58. Christensen, R. M. 1982. Theory of Viscoelasticity. Academic Press, New York.

59. Peng, G., T. Zhang, …, Y. Huan. 2012. Determination of shear creep compliance of linear viscoelastic-plastic solids by instrumented indentation. *Polym. Test.* 31:1038–1044.

60. Chyasnavichyus, M., S. L. Young, and V. V. Tsukruk. 2014. Probing of polymer surfaces in the viscoelastic regime. *Langmuir.* 30:10566–10582.

61. Oliver, W. C., and G. M. Pharr. 1992. An improved technique for determining hardness and elastic modulus using load and displacement sensing indentation experiments. *J. Mater. Res.* 7:1564–1583.

62. Lee, E. H., and J. R. M. Radok. 1960. The contact problem for viscoelastic bodies. *J. Appl. Mech.* 27:438–444.

63. Bilodeau, G. G. 1992. Regular pyramid punch problem. *J. Appl. Mech.* 59:519–523.

64. Popov, V. L., and M. Heß. 2015. Method of Dimensionality Reduction in Contact Mechanics and Friction. Springer, Berlin, Germany.

65. Graham, G. A. C. 1965. The contact problem in the linear theory of viscoelasticity. *Int. J. Eng. Sci.* 3:27–46.

66. Ting, T. C. T. 1966. The contact stresses between a rigid indentor and a viscoelastic half space. *J. Appl. Mech.* 33:845–854.

67. Greenwood, J. A. 2010. Contact between an axisymmetric indenter and a viscoelastic half-space. *Int. J. Mech. Sci.* 52:829–835.

68. Harris, A. R., and G. T. Charras. 2011. Experimental validation of atomic force microscopy-based cell elasticity measurements. *Nanotechnology.* 22:345102.

69. Stamenović, D., N. Rosenblatt, …, D. E. Ingber. 2007. Rheological behavior of living cells is timescale-dependent. *Biophys. J.* 93:L39–L41.